A HR-TEM study on two generations of magnetite from the Alemao IOCG deposit, Carajás, Brazil: Implication for Fe-Cu mineralization

Xiao-Wen Huang [a,b,c,*], Georges Beaudoin [b,c], Yiping Yang [d]

[a] State Key Laboratory of Ore Deposit Geochemistry, Institute of Geochemistry, Chinese Academy of Sciences, Guiyang 550081, China
[b] Département de géologie et de génie géologique, Université Laval, Québec, QC G1V 0A6, Canada
[c] Research Center on the Geology and Engineering of Mineral Resources (E4m), Université Laval, Québec, QC G1V 0A6, Canada
[d] CAS Key Laboratory of Mineralogy and Metallogeny/Guangdong Provincial Key Laboratory of Mineral Physics and Materials, Guangzhou Institute of Geochemistry, Chinese Academy of Sciences, Guangzhou 510640, China

ABSTRACT

Multiple generations of magnetite are common in many magmatic-hydrothermal Fe deposits, which can be formed by different mechanisms. This study investigates magnetite from the Alemao IOCG deposit (Brazil) characterized by inclusion-rich cores (Mag-1) and inclusion-poor rims (Mag-2), using electron probe microanalyzer and high-resolution transmission electron microscopy (HRTEM), to understand its formation mechanism and implications for Fe and Cu mineralization. Electron probe microanalysis shows that Mag-1 has Si and Mg contents of 0.28–1.15 wt% and 0.11–0.49 wt%, respectively, higher than Mag-2. Mineral nanoinclusions of minnesotaite, chlorite, quartz, and minor Ti-rich magnetite in the Mag-1 account for the relatively high Si and Mg in the Mag-1, as measured by electron probe microanalysis. The crystal orientation of nanoinclusions relative to the host Mag1 indicates formation by growth entrapment, where they crystallized from boundary layer supersaturated fluids under non-equilibrium conditions.

Identification of a reaction front, spatial coupling of parent and product phases at micro- and nano-meter scales support the formation of Alemao Mag2 by coupled dissolution and reprecipitation (CDR). Variations in fluid composition rather than fluctuations in conditions such as temperature and oxygen fugacity are the factors inducing CDR. A conceptual model is proposed for the formation of Alemao magnetite where Fe-rich fluids formed inclusion-rich primary magnetite and CDR reactions modified the texture and chemical composition of primary magnetite to form a core rich, and a rim poor, in nanoinclusions. During CDR, impurities of Si, Ca, Al, Mn, and Mg and nanoinclusions are removed from the primary magnetite and formed product magnetite with higher Fe. The progressive enrichment of Cu from Mag-1 to Mag-2 during CDR indicates that a Cu-rich fluid related to the Cu-Au mineralization is responsible the formation of Cu-rich Mag-2 and chalcopyrite. Therefore, micron- to nano-scale characterization of magnetite with multiple generations can provide important constraints on fluid evolution in ore system.

1. Introduction

Magnetite is an important indicator mineral because its widespread occurrence from rocks to ore and because it is resistant to physical abrasion and chemical modification in the surficial environment. Trace elements in magnetite are sensitive to the changes of its precipitation environment, and thus are used to fingerprint different types of mineralization (e.g., Dupuis and Beaudoin, 2011; Nadoll et al., 2014). However, significant variations of trace elements within a magnetite grain have complicated the discrimination of different deposit types using

trace element composition (Dare et al., 2015; Hu et al., 2015; Huang and Beaudoin, 2019, 2021). Magnetite grains with highly variable chemistry commonly have oscillatory or irregular chemical zoning expressed by dark and light gray zones in BSE imaging or major and trace element mapping. The formation of these magnetite textures and the relation with Fe and Cu mineralization remains a matter of debate.

Fluid-rock and fluid-mineral interactions are important mechanisms for the formation of hydrothermal-related deposits such as skarn, iron oxide-copper–gold (IOCG), and Kiruna-type iron oxide-apatite (IOA) deposits (Meinert et al., 2005; Williams et al., 2005; Simon et al., 2018).
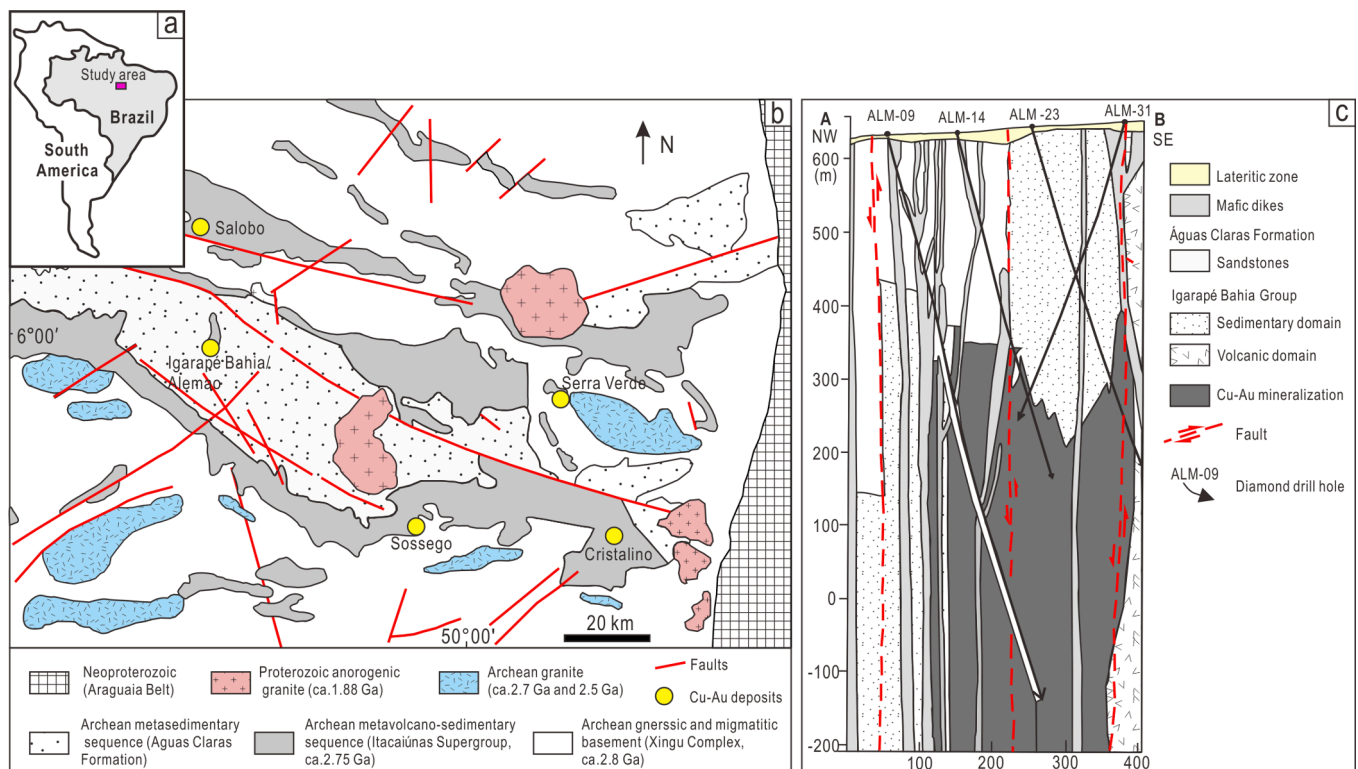
Fig. 1. (a) The location of the Carajás Mineral Province in Brazil. (b) Simplified geological map showing the distribution of major Cu-Au deposits in the northern part of the Carajás Mineral Province in Brazil (modified from Dreher et al., 2005). (c) Cross section of the Alemao deposit (modified from Ronzê et al., 2000).

Magnetite, the main ore mineral in these deposits, records the fluid-mediated mineral reactions. During fluid-magnetite replacement, primary magnetite can partly or completely dissolve, resulting in the formation of secondary magnetite with different compositions. Studies using high-resolution transmission electron microscopy (HRTEM) provide important constraints on the element and mineral behavior during fluid-mineral replacement (Yin et al., 2017; Ciobanu et al., 2019; Yin et al., 2019; Huang and Beaudoin, 2021; Zhou et al., 2021).

In this study, we report micro- to nano-meter scale textural and compositional data of a well-studied magnetite from the Alemao IOCG deposit, Brazil (Huang and Beaudoin, 2019), using electron probe microanalyzer (EPMA) and HRTEM. A large number of nanoinclusions are identified in the trace element-rich cores with various morphology and chemical composition. The formation mechanism of these nano-inclusions and multiple generations of magnetite are discussed with its implication for Fe and Cu mineralization.

2. Geology and sample information

The Carajás mineral province in the northern Brazil hosts numerous IOCG deposits, including Salobo, Igarapé Bahia/Alemao, Cristalino, and Serra Verde (Fig. 1a and b). Sample in this study is collected from the Alemao IOCG deposit (170 Mt @ 1.5% Cu and 0.8 g/t Au) (Fig. 1b; Ronzê et al., 2000). The Alemao deposit consists of Cu-Au mineralization that shares features with the neighboring Igarapé Bahia Cu-Au deposit, including host rocks, hydrothermal alteration, and mineralization styles. The Alemao orebody is 500 m long, 50–200 m wide and strikes at N45°E. The orebody is located at the contact between a lower metavolcanic unit and an upper clastic metasedimentary unit with volcanoclastic rocks (Fig. 1c). Hydrothermal alteration and mineralization at Alemao include early to late Fe-rich metasomatism, chloritization, biotitization, sulfidation, and carbonatization (Ronzê et al., 2000). The extensive Fe-rich metasomatism is characterized by magnetite, Fe-rich

chlorite, grunerite, cummingtonite, siderite, and greenalite (Ronzê et al., 2000). Chlorite is present in both mineralized and barren zones, which are Fe-rich and Mg-rich, respectively. Sulfide stage minerals include chalcopyrite, pyrite, pyrrhotite with minor molybdenite, galena, digenite, covellite, and bornite. The paragenesis of carbonate stage is siderite, ankerite, and calcite. There are two types of ores. The first type is composed of bands of magnetite and chalcopyrite and breccias of volcanics, tuffs, and banded iron formation within the matrix of magnetite, chalcopyrite, and alternation minerals. The second type of ore consists of brecciated, altered volcanic rocks associated with chalcopyrite, bornite, pyrite, chlorite, siderite and ankerite. Hydrothermal fluids rich in CO_2, F, and Cl are responsible for the Cu-Au mineralization and REE enrichment (Ronzê et al., 2000). The petrography and chemical composition of the selected magnetite sample from Alemao have been reported in Huang et al. (2019) and Huang and Beaudoin (2019). The ore is composed of ~80% chalcopyrite, ~15% magnetite and ~5% other minerals. The sample Alemao selected for HRTEM has a mineral assemblage of magnetite, chlorite, apatite, chalcopyrite, and calcite (Fig. 2a and b). A number of magnetite grains in this sample are composed of an inclusion-rich core overgrown by an inclusion-poor rim (Fig. 2b). The core-rim texture has been interpreted as the product of coupled dissolution and reprecipitation (CDR; Huang and Beaudoin, 2019).

3. Analytical methods

3.1. EPMA analyses

Magnetite petrography was characterized by optical microscopy and back-scattered electron (BSE) imaging before major and minor element analyses at Université Laval using a CAMECA SX-100 electron probe microanalyzer (EPMA). Chemical composition of magnetite was analyzed using the same conditions as those described by Huang and
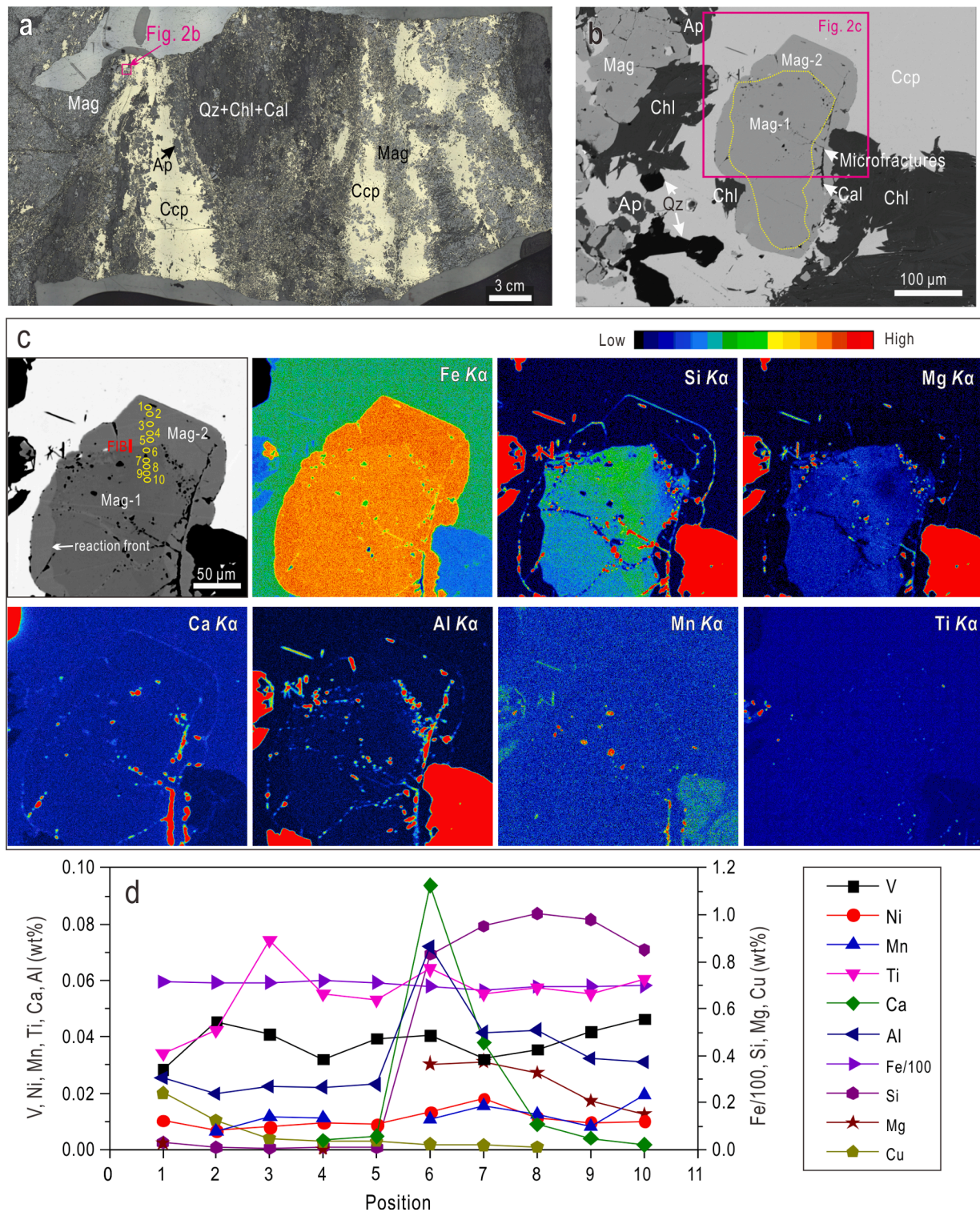
Fig. 2. (a) Thin section scan showing the major mineral assemblage of ore sample from the Alemao IOCG deposit (Brazil) and the location of studied magnetite. Magnetite and apatite were replaced by chalcopyrite, quartz, chlorite, and calcite. (b) Back-scattered electron (BSE) image of the selected area composed of magnetite, chlorite, apatite, chalcopyrite, and quartz. Minor calcite occurs as veins in magnetite. Magnetite has core-rim textures that are composed of dark gray core (Mag-1) and light gray rim (Mag-2). (c) BSE image and energy dispersive X-ray maps of Alemao magnetite. Magnetite foil prepared by Focused Ion Beam (FIB) crosscuts the boundary between dark gray and light gray zones. The dark gray core of magnetite has higher Si and Mg but lower Fe contents than the light zone. It should be noted that Si and Mg are not homogenously distributed in the dark gray core where Si-Mg-rich zone is observed. There are no obvious differences in Ca, Al, Mn, and Ti contents between core and rim. Some silicate inclusions in magnetite can be identified by relatively high Si, Mg, and Al contents, whereas some carbonate inclusions can be recognized by relatively high Ca and Mn contents. (d) Major and trace element composition of Alemao magnetite. Notes that the dark gray core (Points 1 to 5) has higher Si, Mg, and Al, but slightly lower Cu contents than the light gray rim (Point 7 to 10). Elevated Ca and Al contents of point 6 in the dark gray core are likely due to contamination of silicate inclusions. Iron, V, Ni, and Mn contents are similar between core and rim. Mineral abbreviations: Ap = apatite, Cal = calcite, Ccp = chalcopyrite, Chl = chlorite, Mag = magnetite, Qz = quartz.
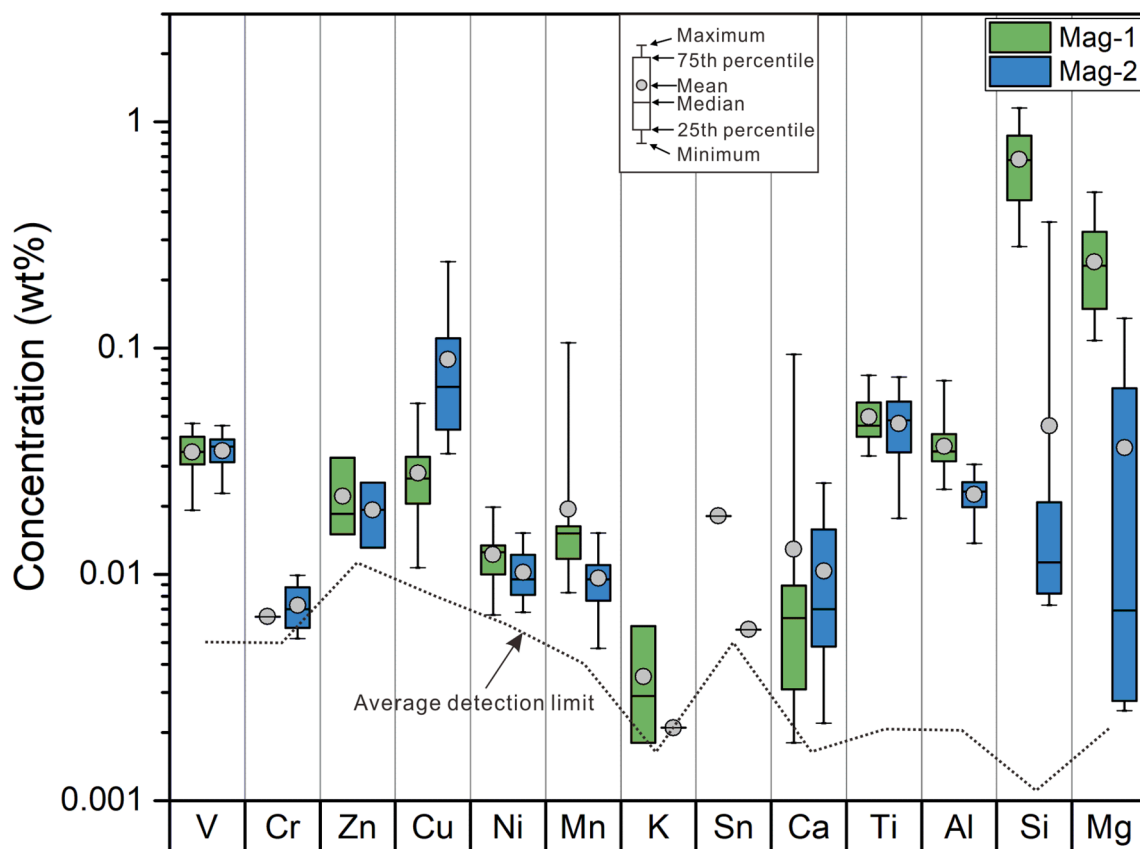
Fig. 3. Box and whisker plots for electronic probe element data showing the compositional differences between dark gray core (Mag-1) and light gray rim (Mag-2) in Alemao magnetite. Data below the limit of detection were not considered in this plot.

Beaudoin (2019), including using a 5-μm diameter beam, a 15 kV voltage, a current of 20nA for Fe and of 100nA for minor and trace elements. A series of natural and synthetic standards, simple oxides (GEO Standard Block of P and H Developments) and natural minerals (Mineral Standard Mount MINM 25–53, Astimex Scientific), are used to calculate the element concentrations. The integration time for X-ray peak collection is 15–20 s for background and 20–40 s based on different elements. Average detection limits are 463 ppm for Fe, 110 ppm for Zn, 84 ppm for Cu, 62 ppm for Ni, 41–53 ppm for V, Cr, Mn, and 14–33 ppm for K, Ca, Ti, Al, Si, Mg, and P. Element maps with a resolution of 512×512 pixels are acquired using a 1 μm beam, 15 kV accelerating voltage, 100nA beam current, and a counting time of 20 ms for each pixel.

3.2. HRTEM analyses

A foil suitable for HRTEM was prepared at the Canadian Center for Electron Microscopy (CCEM), McMaster University, using a Helios G4 PFIB UXe DualBeam (Xeon Plasma Focused Ion Beam, Thermo Scientific, Hillsboro, USA). Protected initially by electron deposited Pt + C followed by the Xe deposition, a foil of approximately $20×15×1$ μm^3 was in-situ cut from the magnetite grain in the polished thin section using a 30 kV Xe ion beam. The thin foil was then glued to Cu grids, and was thinned to become electronically transparent with progressively reduced currents from 1.0 to 0.3nA at 30 kV and polished with low kV beams (>2 kV).

A FEI Titan 80–300 TEM at CCEM, equipped with CEOS image corrector, was used to characterize the type and distribution of nano-inclusions in the magnetite foil. The TEM is equipped with a Tridiem imaging filter (Gatan), a high-angle annular dark field detector (HAADF, Fishione), and an energy dispersive X-ray spectrometry (EDS, Oxford Instruments) with ultrathin window. X-ray data was collected at an acceleration voltage of 200 kV, using an acquisition time of 120 s and 2 h for point analysis and elemental maps, respectively. Diffraction patterns of nanoinclusions and magnetite matrix are obtained from HRTEM images by fast Fourier transform (FFT).

4. Results

4.1. Chemistry of Alemao magnetite

Element maps show that the dark gray, inclusion-rich core (Mag-1) has higher Si and Mg but lower Fe contents than the light gray, inclusion-poor rim (Mag-2) (Fig. 2c). Moreover, Si and Mg are heterogeneously distributed in the core with a Si-Mg-rich zone (Fig. 2c). There are no obvious differences in Ca, Al, Mn, and Ti contents in the core (Fig. 2c). Point analysis along a line perpendicular to the contact between the inclusion-rich core and inclusion-poor rim shows higher Si, Mg, and Al contents characterize the inclusion-rich core (Fig. 2d). Titanium and V are heterogeneously distributed but without obvious differences between two zones (Fig. 2d). Integrating EPMA data from this study and Huang and Beaudoin (2019), Mag-1 has higher average Mn, K,
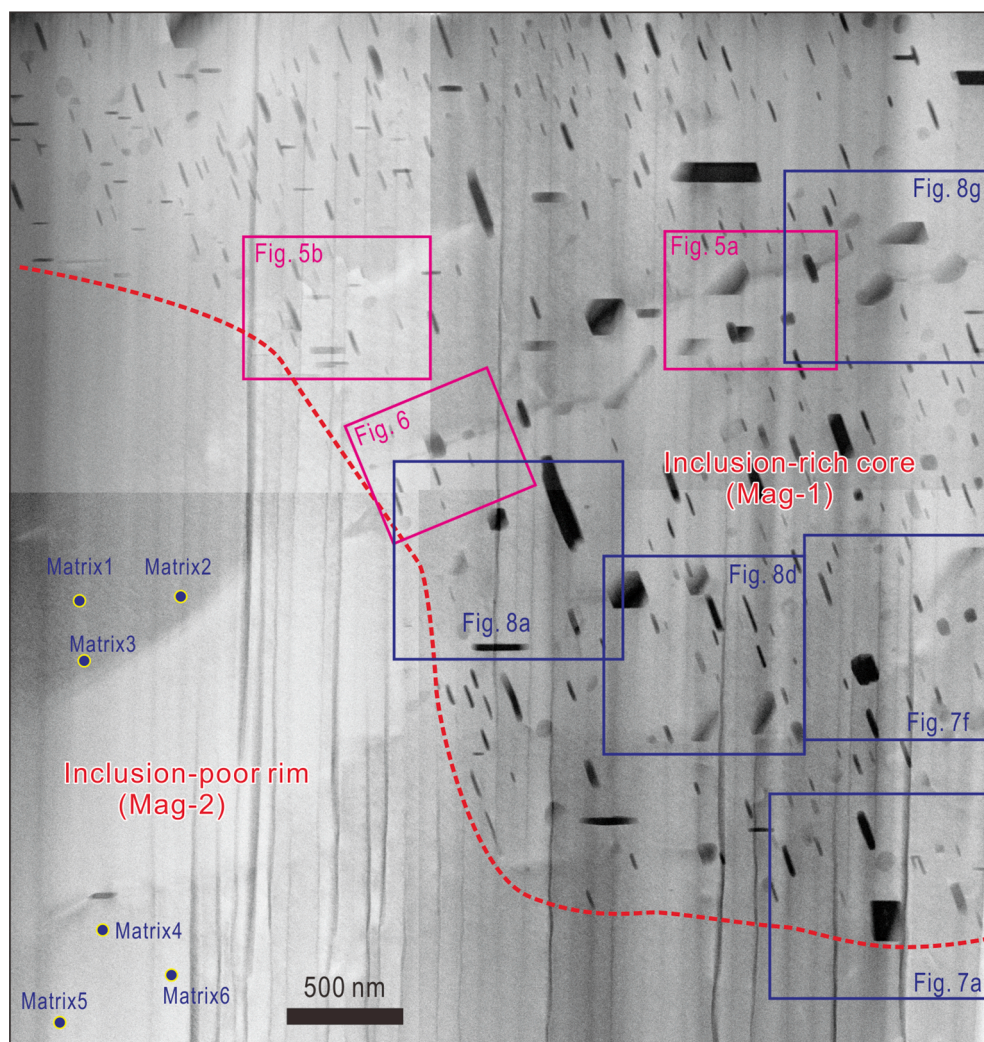
Fig. 4. HAADF image of magnetite foil ($\sim$4.1$\times$4.4 μm) prepared by FIB sampling. This image is spliced by four separated images, resulting in some differences in gray levels. The boundary between inclusion-rich core and inclusion-poor rim is marked by red dotted lines. The inclusion-rich core and inclusion-poor rim correspond to the dark gray and light gray zones in BSE image of Fig. 2c. The selected areas for TEM-EDS mapping are marked by red rectangles, whereas point analyses and HRTEM images are marked by blue rectangles. Note that no porosity is observed in magnetite and most of minerals have the similar crystal orientation. Blue filled circles marked with Matrix1 to Matrix6 in the inclusion-poor rim mean TEM-EDS point analyses. Chemical data of these point analyses can be seen in Appendix Table 2.

Ca, Al, Si, and Mg contents but lower average Cu content than Mag-2 (Fig. 3), with differences in average Si and Mg contents up to one order of magnitude (Fig. 3). Mag-1 has Si and Mg contents of 0.28–1.15 wt% and 0.11–0.49 wt%, respectively, whereas Mag-2 has contents of 0.01–0.36 wt% Si and from below detection limit to 0.14 wt% Mg (Appendix Table 1). Iron contents of Mag-1 range from 63.3 to 70.5 wt% with an average of 69.1 wt%, whereas that of Mag-2 are 62–71.7 wt%, averaging at 70.2 wt% (Appendix Table 1). Average V, Cr, Zn, Ni, and Ti contents are similar between two zones (Fig. 3).

4.2. Chemistry of nanoinclusions and magnetite matrix

Nanoinclusions are common in the inclusion-rich core and absent in the rim (Fig. 4). There is no significant compositional difference between magnetite matrix in inclusion-rich core and inclusion-poor rim (Fig. 4). TEM-EDS mapping, point analyses and HRTEM imaging have identified five mineral nanoinclusions in the inclusion-rich core of Alemao magnetite: 1) minnesotaite (Fe$_{2.5}^{2+}$Mg$_{0.5}$Si$_4$O$_{10}$(OH)$_2$), 2) chlorite, 3) quartz, 4) talc, 5) Ti-rich magnetite (Figs. 5-8). These nanoinclusions show different crystal orientation relative to the host magnetite (Fig. 4).

TEM-EDS mapping of the selected areas shows that Fe, Si, Mg, Al, and Ti contents are relatively homogenous in the magnetite matrix of the inclusion-rich core (Fig. 5a and b and Fig. 6). This indicates that the heterogeneous distribution of Si, Mg, and Al in the inclusion-rich core (Fig. 2c) is mainly due to irregular distribution of nanometer mineral inclusions.

Minnesotaite is widespread in the inclusion-rich zone with variable morphology and composition. Minnesotaite is mainly prismatic (Fig. 7a) and, in some cases, cubic (Fig. 7f), and can be identified by elevated Fe, Si, and Mg contents. Minnesotaite shows a clear contact with the magnetite matrix (Fig. 7b, d and g) and has a different crystal structure from magnetite (Fig. 7c, e and h). The minnesotaite has an epitaxial growth relationship with the magnetite matrix as shown by the [001] axis of minnesotaite that is parallel to the [111] aixs of magnetite (Fig. 7c). Two chlorite nanoinclusions are identified in the studied area of the foil by elevated Si, Mg, and Al contents compared to magnetite matrix (Fig. 5b and Fig. 8a). One larger chlorite is $\sim$550$\times$160 nm (Fig. 8a), and shows an abrupt contact with the magnetite matrix, with a different crystal structure (Fig. 8b and c). HRTEM image shows a lattice fringe of 1.4 nm corresponding to the TOTO unit cell of chlorite. The
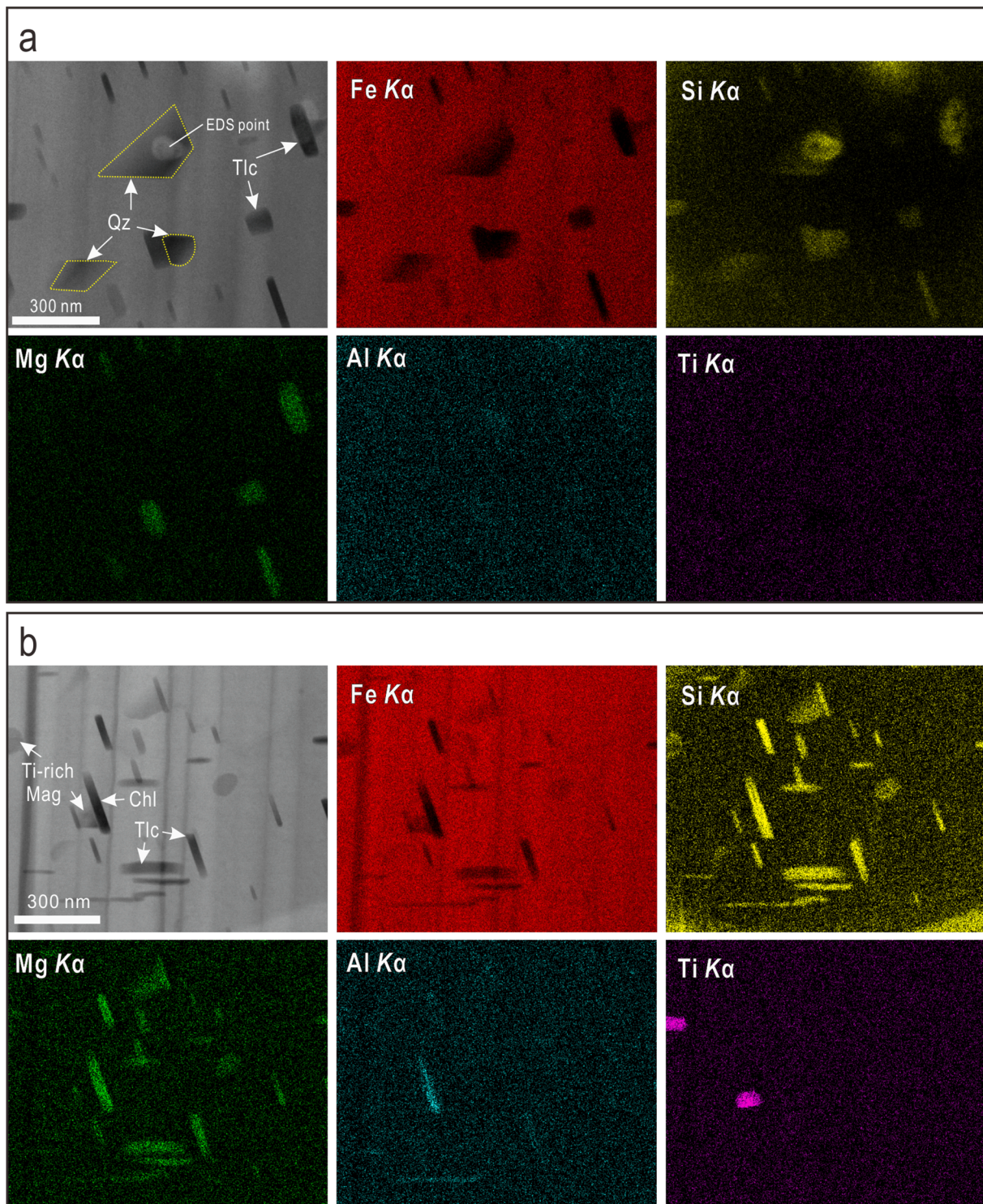
Fig. 5. (a) HAADF image and corresponded TEM-EDS element maps of magnetite showing that the distribution of element and nanoinclusions in inclusion-rich core. Relatively homogenous distribution of elements Fe, Si, Mg, Al, and Ti is observed in the magnetite matrix. Quartz nanoinclusions with euhedral crystals are identified by elevated Si contents, whereas talc nanoinclusions are recognized by elevated Si and Mg contents. (b) HAADF image and corresponded TEM-EDS element maps of inclusion-rich core in Alemao magnetite. Elements Fe, Si, Mg, Al, and Ti are homogenously distributed in the magnetite matrix. Talc nanoinclusions are characterized by relatively high Fe, Si, and Mg contents, whereas chlorite nanoinclusions are identified by elevated Fe, Si, Mg and Al contents. Two Ti-rich magnetite nano-inclusions are also observed due to relatively high Ti contents (~13.8 wt% and ~8.8 wt%). Mineral abbreviations: Chl = chlorite, Mag = magnetite, Qz = quartz, Tlc = talc.
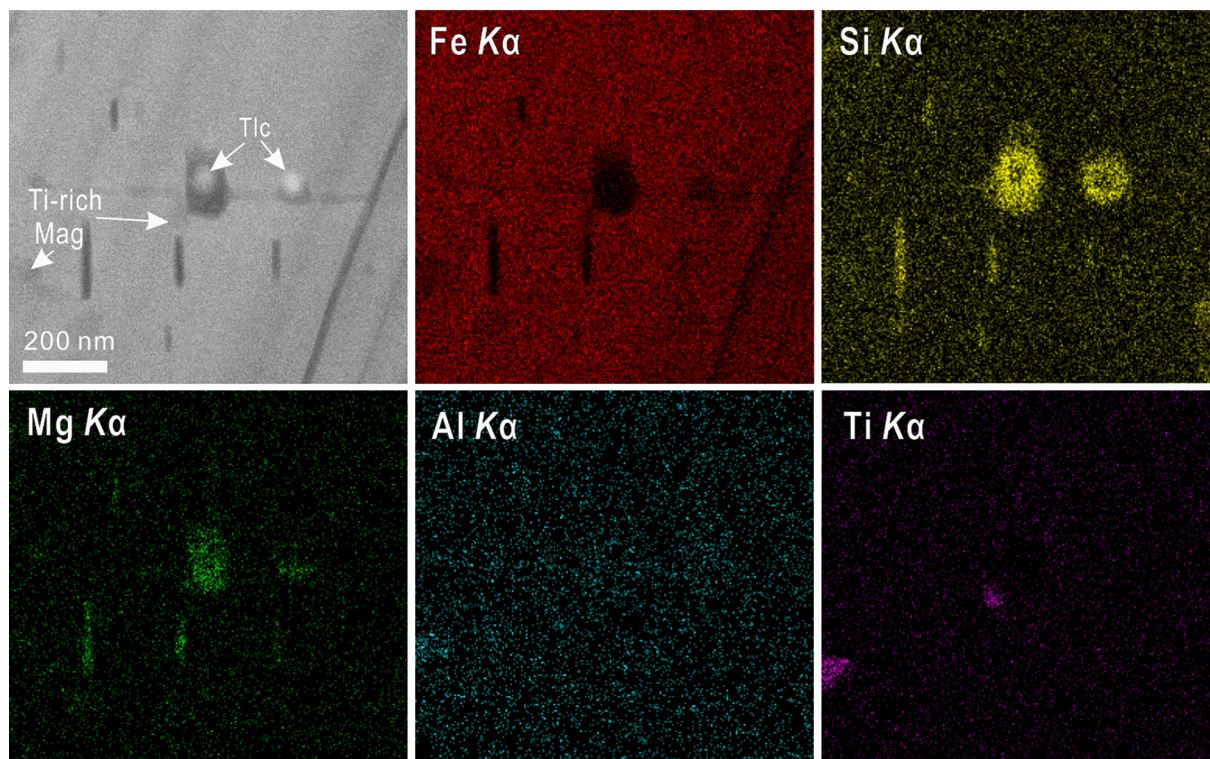
Fig. 6. HAADF image and corresponded TEM-EDS element maps of selected area in the inclusion-rich core. Relatively high Si and Mg contents compared to magnetite matrix indicate talc nanoinclusions, whereas relatively high Ti content identifies Ti-rich (~6.4 wt% Ti) magnetite nanoinclusions. Mineral abbreviations: Mag = magnetite, Tlc = talc.

sharp and bright FFT pattern along [010] zone axis further confirms a well-crystallized chlorite-1 *M* inclusion (Fig. 8c).

Quartz is cubic, prismatic, or hexagonal (Fig. 5a, Fig. 6, Fig. 8d and g) and can be identified by elevated Si contents compared to magnetite matrix (Fig. 5a). The boundary between quartz and magnetite is abrupt (Fig. 8e and h). The FFT patterns of magnetite along [011] zone axis and quartz along [1 1 1] zone axis are similar, indicating an epitaxial growth relationship with magnetite matrix (Fig. 8f and i).

Talc is prismatic (Fig. 5a and b, Fig. 6, Fig. 8a, d and g), and can be identified by elevated Si and Mg contents than the magnetite matrix (Fig. 5a and b, Fig. 6). Four Ti-rich magnetite nanoinclusions are identified by TEM-EDS in the inclusion-rich core (Fig. 5b, Fig. 6). The titaniferous magnetite is composed of 59.9–69.5 wt% Fe and 6.3–13.8 wt% Ti (Appendix Table 2).

TEM-EDS analyses of the magnetite matrix in the inclusion-poor rim (Matrix 1 to 6, Fig. 4) show that it contains 14.4–20.6 wt% Si and 43.5–53.7 wt% Fe (Appendix Table 2). Two analyses of magnetite matrix in the inclusion-rich core (Matrix 7, 8, Fig. 7f) show that they have chemical composition close to pure magnetite (Appendix Table 2).

5. Discussion

5.1. Formation of nanoinclusions

The Alemao magnetite has a close association with apatite, chlorite, quartz, and calcite, indicating that it formed by hydrothermal alteration related to iron-rich metasomatism, chloritization, and carbonatization (Ronzê et al., 2000). Chalcopyrite occurs as veins filling fractures in magnetite (Fig. 2a) and magnetite is enclosed in chalcopyrite (Fig. 2b), indicating that magnetite formed earlier than chalcopyrite. The amounts of minnesotaite, quartz, talc and chlorite nanoinclusions in Mag-1 are consistent with chlorite and quartz assemblages at the thin section scale (Fig. 2b), indicating that these nanoinclusions are also formed by hydrothermal processes.

Ti-rich (6.3–13.8 wt% Ti) magnetite nanoinclusions in Mag-1 (Fig. 5b, 6) are similar to Ti-rich magnetite (6.2–16 wt% Ti) nanoinclusions in hydrothermal magnetite from Los Calorados iron oxide-apatite deposit in Chile (Deditius et al., 2018), which was possibly composed of magnetite-ulvöspinel intergrowths. EPMA analyses show that Mag-1 has an average Ti content of ~0.06 wt%, similar to Los Calorados magnetite with Ti content of <0.3 wt% (Deditius et al., 2018). Both Mag-1 from the Alemao IOCG deposit and magnetite from Los Calorados IOA deposit have Ti contents lower than the high-Ti (>~1 wt% Ti) magmatic magnetite hosting ilmenite exsolutions (Dare et al., 2012; Liu et al., 2015), indicating that fluids responsible for these magnetite samples are Ti-undersaturated.

The presence of silicate and Ti-rich magnetite nanoinclusions in the inclusion-rich core (Mag-1) indicates that hydrothermal fluids were locally supersaturated relative to these nanominerals (Deditius et al., 2018). The regular crystal orientation of these nanoinclusions (Fig. 4) is consistent with the growth entrapment model (Watson, 1996; Watson et al., 2011; Deditius et al., 2018), where nanominerals are formed from fluids in the boundary layer under non-equilibrium condition. This growth model is different from ilmenite exsolution in Ti-rich magnetite which is a sub-solidus re-equilibration process where decreasing temperature and changing oxygen fugacity results in decreased solubility of
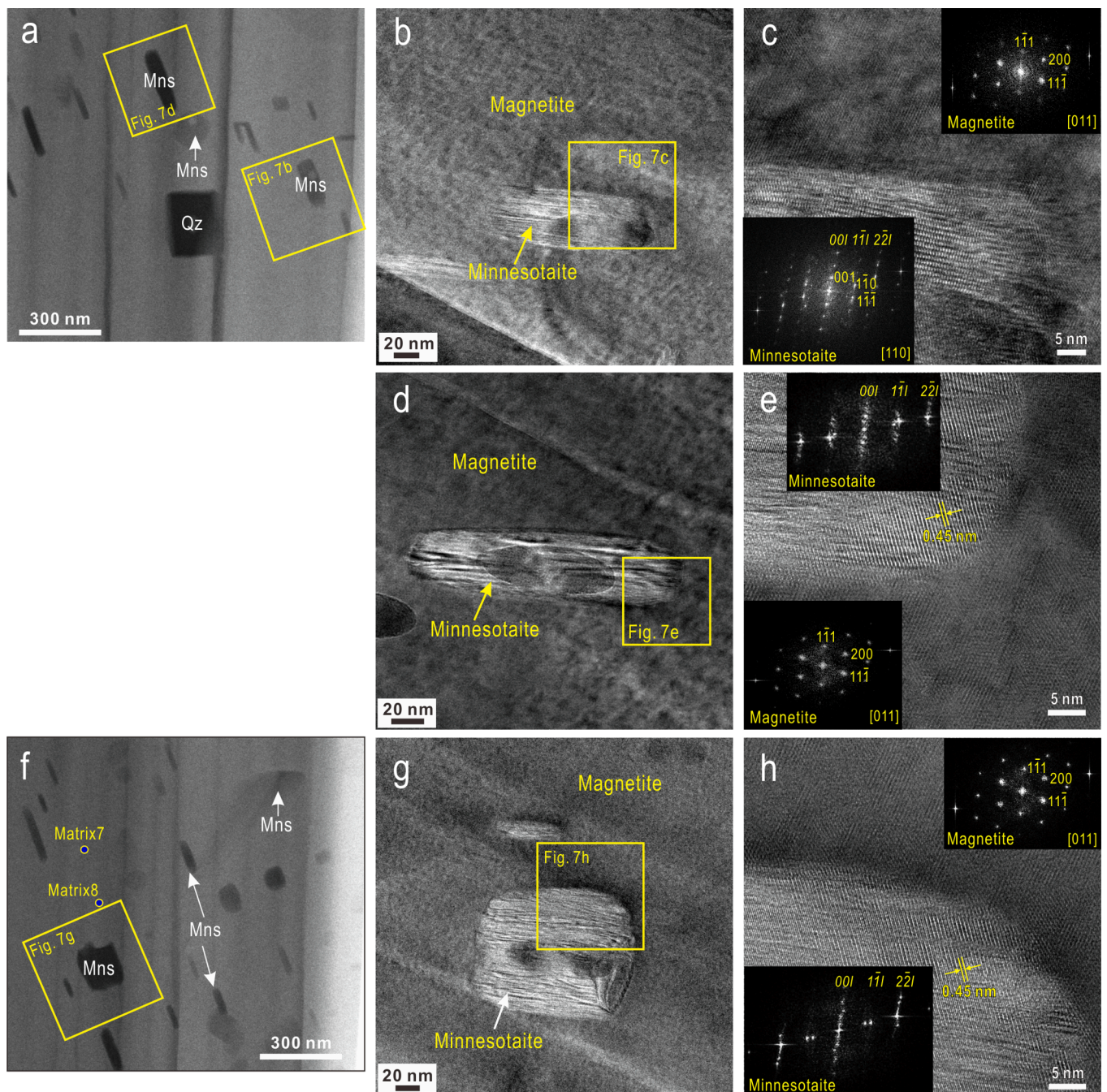
Fig. 7. (a, f) HAADF image showing nanoinclusions of minnesotaite with different morphologies. (b, d, g) Bright-field, low-magnification TEM images of minnesotaite in magnetite. (c, e, h) HRTEM images of the grain boundary between minnesotaite and host magnetite. Matrix 7 and 8 represent the point analyses of the host magnetite, and the EDS data are shown in Appendix Table 2. Note that prismatic (b, d) and cubic (g) minnesotaite have similar crystal structures as indicated by FFT patterns. Mineral abbreviations: Mns = minnesotaite, Qz = quartz.

Ti in magnetite and causes redistribution of Ti in co-crystallized phases (Frost and Lindsley, 1991). Therefore, both silicate and Ti-rich magnetite nanoinclusions most likely crystallized from bulk-undersaturated fluids that became supersaturated in the boundary fluid layer under non-equilibrium or far from equilibrium conditions. Similar scenario is also observed in Au-bearing magnetite in the Beiya Au deposit, China (Zhou et al., 2017). Gold commonly has an affinity with sulfides, but abundant gold micro- to nano-meter inclusions in magnetite demonstrate that Au can be enriched from the gold-undersaturated fluids in the magnetite boundary layer (Zhou et al., 2017).

5.2. Formation of Alemao magnetite by coupled dissolution and reprecipitation

Zoned magnetite can form by different processes. Magnetite with oscillatory zoning is commonly interpreted to result from cyclic fluctuations in fluid composition, temperature or oxygen fugacity (Dare et al., 2015; Knipping et al., 2015; Deditius et al., 2018; Huang et al., 2018; Huang and Beaudoin, 2019). Huang and Beaudoin (2021) interpreted oscillatory zoning in magnetite from the Sossego IOCG deposit, Brazil as a result of a self-organization process where variable fluid composition is a feedback response for an evolving fluid system far from equilibrium, rather than the variations in temperature and oxygen fugacity. However,
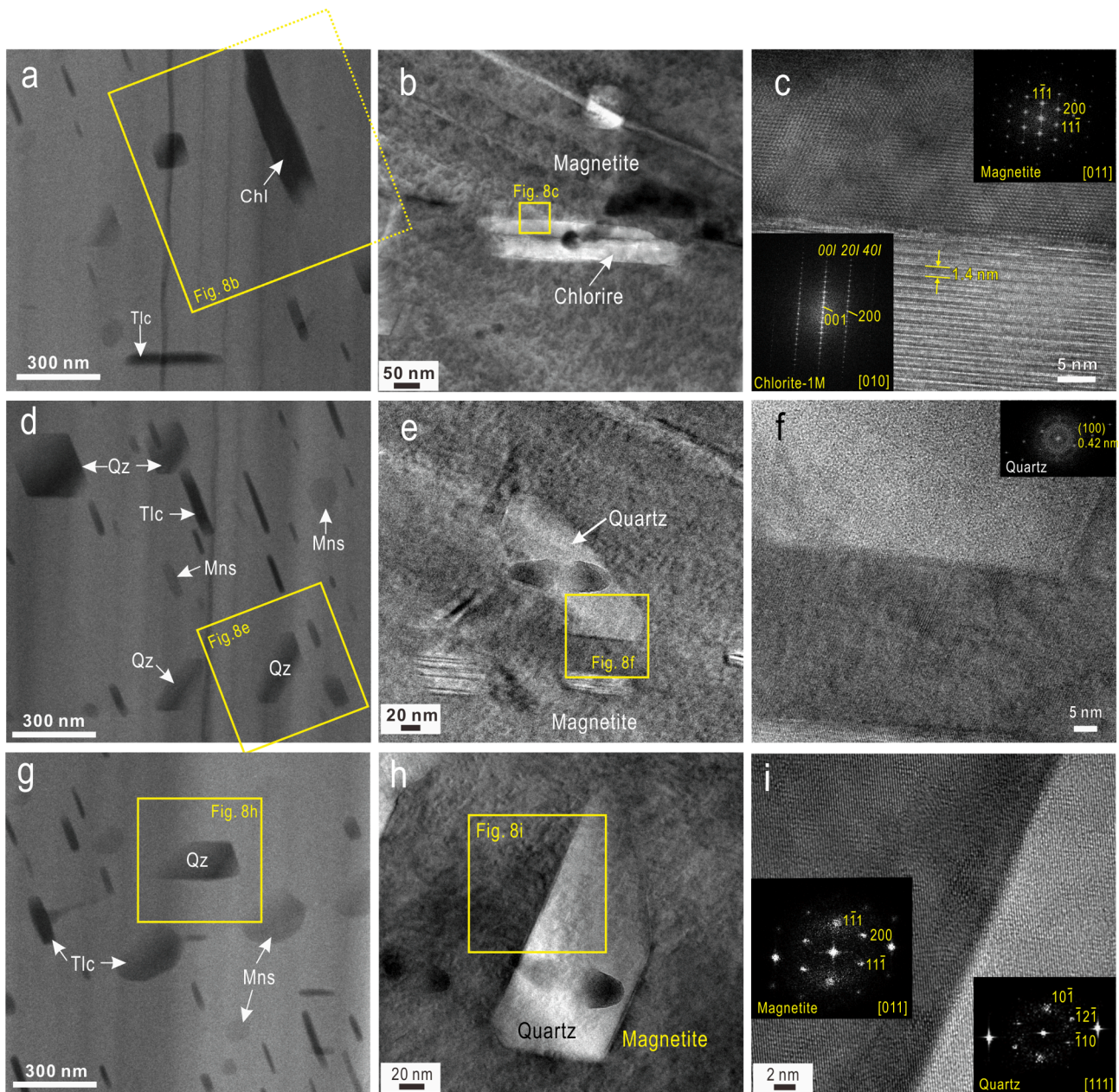
Fig. 8. (a, d, g) HAADF image showing nanoinclusions of chlorite and quartz in the inclusion-rich zone. Chlorite is prismatic, whereas quartz is mostly hexagonal. (b, e, h) Bright-field, low-magnification TEM images of nanometer minerals in magnetite. (c, f, i) HRTEM images showing clear boundary between chlorite, quartz and host magnetite. Mineral abbreviations: Chl = chlorite, Mns = minnesotaite, Qz = quartz, Tlc = talc.

oscillatory zoning in magnetite from the Baishiya iron skarn deposit was interpreted as the product of CDR (Yin et al., 2017; Yin et al., 2019), where replicate formation of Al-rich magnetite, Al-rich nanometer-sized lamellae, and zinc spinel nanoparticles in the reaction front results in the trace element-rich zones.

The sharp reaction front between Mag-1 and Mag-2 (Fig. 2c) is a typical feature of CDR (Putnis, 2009; Altree-Williams et al., 2015). The different Si-Mg-rich zones in the magnetite core (Mag-1; Fig. 2c) indicate that silicate nanoinclusions are heterogeneously distributed in Mag-1. Because Mag-1 and Mag-2 occur as parts of a single magnetite grain

and texture suggests replacement of Mag-1 by Mag-2 (Fig. 2b), Mag-2 was most likely formed by dissolution of Mag-1 by fluid-magnetite reaction. Interconnected pores commonly develop in the product phase during CDR and facilitate fluid infiltration (Putnis, 2015). No nanometer-scale pores are found in both Mag-1 and Mag-2 (Figs. 4-8). This is consistent with the transient feature of porosity during CDR (Putnis, 2015).

Similar Ti and V contents between inclusion-rich Mag-1 and inclusion-poor Mag-2 (Fig. 3) indicate that temperature and oxygen fugacity are not important factors controlling the formation of Alemao
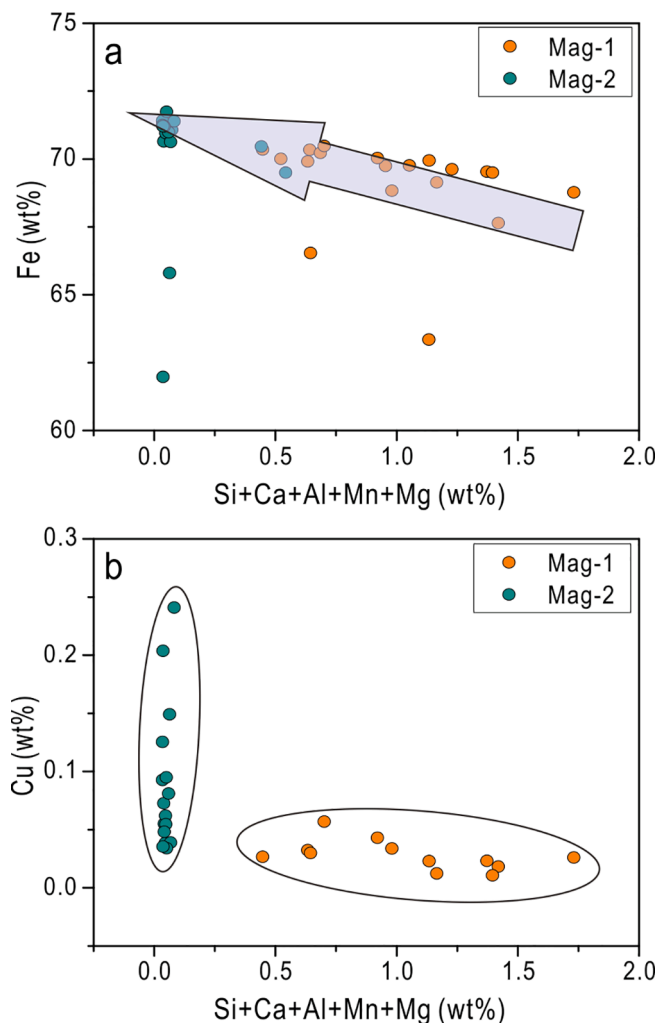
Fig. 9. Plot of Si + Ca + Al + Mn + Mg versus Fe and Cu for different domains of magnetite from the Alemao deposit.

magnetite. The magnetite matrix of inclusion-rich core (Mag-1) has chemical composition close to pure magnetite but contains nano-inclusions of silicates, indicating that Si, Mg, Ca, and Al became saturated in the boundary layer by precipitation of pure magnetite matrix where it formed the silicate nanoinclusions. In contrast, magnetite matrix of inclusion-poor rim (Mag-2) contains elevated Si, indicating that Si is undersaturated and can be incorporated into the structure of magnetite. Therefore, the differences in contents and occurrences of fluid-mobile elements such as Si, Mg, Ca, and Al between Mag-1 and Mag-2 demonstrate that variation in fluid composition plays a more important role in the formation of Alemao magnetite.

5.3. Implication for Fe and Cu mineralization

Two generations of magnetite from the Alemao IOCG deposit with different chemical and mineral compositions records fluid evolution during Fe and Cu mineralization. From Mag-1 to Mag-2, Si, Ca, Al, Mn, and Mg contents decrease, whereas Fe and Cu contents increase (Fig. 9a and b). This indicates that CDR process can slightly increase the Fe grade in magnetite by removing impurities of Si, Ca, Al, Mn, and Mg, which is consistent with the results of magnetite from skarn deposits (Hu et al.,

2014; Huang et al., 2018) and other IOCG deposits (Huang and Beaudoin, 2019). Because Cu is an incompatible element in magnetite crystallized from a chloride-rich hydrothermal fluid (Ilton and Eugster, 1989), even trace amounts of Cu in magnetite reflects strong enrichment of Cu in fluids. Mag-1 has Cu content below ~0.05 wt%, lower than Cu content (~0.05–0.25 wt%) of Mag-2 (Fig. 9b). Absence of Cu-bearing mineral nanoinclusions in both Mag-1 and Mag-2 suggests that Cu occurs mainly as solid solution in magnetite. Ilton and Eugster (1989) give the distribution coefficient in magnetite $Kd_{Cu-Fe} = (X_{Cu}/X_{Fe})^{FL}/(X_{Cu}/X_{Fe})^{SS}$, where X_{Cu} and X_{Fe} represent the mole fractions of Cu and Fe, respectively, and FL and SS are the fluid and solid solution, respectively. Using a $Kd = 77000$ for magnetite formed at 650 °C (Ilton and Eugster, 1989), average 69.1 wt% Fe and 0.03 wt% Cu for Mag-1, and 70.2 wt% Fe and 0.09 wt% Cu for Mag-2, calculated $(X_{Cu}/X_{Fe})^{FL}$ yield values for Mag-1 and Mag-2 of 29 and 85, respectively. This is consistent with fluids enriched in Cu in Mag-2 relative to Mag-1. The relative enrichment of Cu in Mag-2 indicates that Cu-rich fluid replacement of Mag-1 in relation to Cu-Au mineralization event results in the precipitation of Cu-rich Mag-2 and associated chalcopyrite. This is consistent with the texture Alemao magnetite surrounded by chalcopyrite at Fig. 2a and b. Therefore, two generations of magnetite, Mag-1 and Mag-2, likely record Fe and Cu mineralization events, respectively, and thus magnetite with core-rim texture is a good tool to unravel fluid evolution in the IOCG system.

5.4. A conceptual model for the formation of Alemao magnetite

Textural and compositional variations during fluid-magnetite reaction are schematically shown for the formation process of two generations of magnetite in Alemao (Fig. 10). Primary magnetite (Mag-1) in Alemao crystallized from Fe-rich hydrothermal fluids responsible for the high-temperature Ca-Fe alteration based on the mineral assemblage of magnetite and apatite (Huang et al., 2019). Fe-rich fluid metasomatism also resulted in the formation of Fe-rich chlorite, Fe-rich amphibole, such as grunerite and cummingtonite, and siderite (Ronzê et al., 2000). Iron, Si, Mg, and Ca nanoinclusions formed in Mag-1 due to local supersaturation in the boundary layer fluids at the surface of Mag-1 (Fig. 10). The inner zoning of Si and Mg in the Mag-1 as shown in EPMA mapping most likely reflects heterogenous distribution of these silicate nanoinclusions (Fig. 2c). The primary magnetite has been affected by Cu-rich fluid replacement events, resulting disequilibrium between inclusion-rich primary magnetite (Mag-1) and fluids, partial dissolution of core Mag-1, and formation of Cu-rich, inclusion-poor rim Mag-2. The Cu-rich fluid replacement also results in the formation of chalcopyrite which represents the main Cu-Au mineralization event. The deformation of magnetite results in fragmentation of the whole grain, forming some small fractures. Later fluid infill and replacement along fractures formed calcite-dominated veins. The combined chemical and physical processes result in the formation of Alemao magnetite with core-rim texture and crosscutting veins.

6. Conclusions

Detailed petrography demonstrates that Alemao magnetite with core-rim texture was characterized by different chemical compositions and nanometer mineralogy. The trace element-rich core (Mag-1) was composed of mineral nanoinclusions, including minnesotaite, chlorite, quartz, and minor Ti-rich magnetite. These nanoinclusions were formed by growth entrapment mechanism due to local supersaturation under non-equilibrium conditions. The inclusion-poor rim (Mag-2) was formed via coupled dissolution-reprecipitation reaction due to various fluid
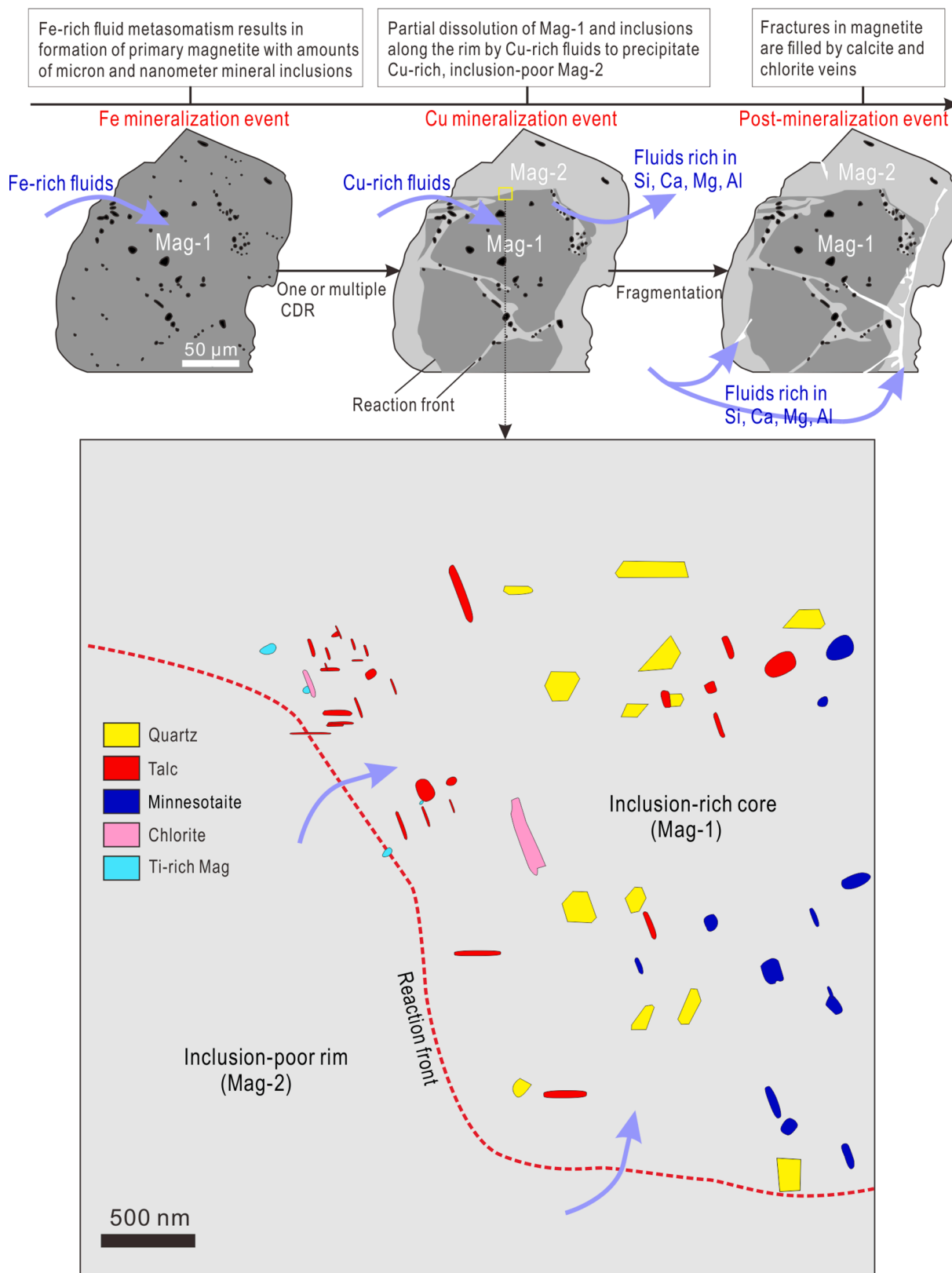
Fig. 10. Simplified cartons showing the formation of Alemao magnetite and nanoinclusions. The formation of two generations of magnetite from the Alemao deposit results from coupled dissolution and reprecipitation (CDR) and fragmentation. See text for more detailed explanation. Mineral abbreviations: Chl = chlorite, Mns = minnesotaite, Mag = magnetite, Qz = quartz, Tlc = talc.

composition rather than fluctuations in temperature and oxygen fugacity. A conceptual model involving one or multiple CDR and fragmentation was proposed for the formation of two generations of magnetite. During CDR, impurities of Si, Ca, Al, Mn, and Mg were removed from primary magnetite to form product magnetite enriched in Fe. The Cu-rich fluid replacement of Mag-1 during Cu-Au mineralization event results in relative enrichment of Cu in Mag-2 and formation of chalcopyrite associated with Mag-2. Therefore, magnetite with core-rim texture records both Fe and Cu mineralization events, and is an important indicator mineral for fluid evolution in IOCG deposits.

Declaration of Competing Interest

The authors declare that they have no known competing financial interests or personal relationships that could have appeared to influence the work reported in this paper.

Acknowledgments

Appendix A. Supplementary data

Supplementary data to this article can be found online at https://doi.org/10.1016/j.oregeorev.2022.104934.

References

Altree-Williams, A., Pring, A., Ngothai, Y., Brugger, J., 2015. Textural and compositional complexities resulting from coupled dissolution–reprecipitation reactions in geomaterials. Earth Sci. Rev. 150, 628–651.

Ciobanu, C.L., Verdugo-Ihl, M.R., Slattery, A., Cook, N.J., Ehrig, K., Courtney-Davies, L., Wade, B.P., 2019. Silician Magnetite: Si–Fe-Nanoprecipitates and Other Mineral Inclusions in Magnetite from the Olympic Dam Deposit. South Australia. Minerals 9, 311.

Dare, S.A.S., Barnes, S.-J., Beaudoin, G., 2012. Variation in trace element content of magnetite crystallized from a fractionating sulfide liquid, Sudbury, Canada: Implications for provenance discrimination. Geochim. Cosmochim. Acta 88, 27–50.

Dare, S.A.S., Barnes, S.-J., Beaudoin, G., 2015. Did the massive magnetite "lava flows" of El Laco (Chile) form by magmatic or hydrothermal processes? New constraints from magnetite composition by LA-ICP-MS. Miner. Deposita 50 (5), 607–617.

Deditius, A.P., Reich, M., Simon, A.C., Suvorova, A., Knipping, J., Roberts, M.P., Rubanov, S., Dodd, A., Saunders, M., 2018. Nanogeochemistry of hydrothermal magnetite. Contrib. Mineral. Petrol. 173, 46.

Dreher, A.M., Xavier, R.P., Martini, S.L., 2005. Fragmental rocks of the Igarapé Bahia Cu-Au deposit, Carajás Mineral Province, Brazil. Brazilian Journal of Geology 35, 359–368.

Dupuis, C., Beaudoin, G., 2011. Discriminant diagrams for iron oxide trace element fingerprinting of mineral deposit types. Miner. Deposita 46 (4), 319–335.

Frost, B.R., Lindsley, D.H., 1991. Occurrence of iron-titanium oxides in igneous rocks. In: Lindsley, D.H. (Ed.), Oxide minerals: petrologic and magnetic significance. Reviews in Mineralogy and Geochemistry, p. 433-468.

Hu, H., Lentz, D., Li, J.-W., McCarron, T., Zhao, X.-F., Hall, D., 2015. Reequilibration processes in magnetite from iron skarn deposits. Econ. Geol. 110 (1), 1–8.

Hu, H., Li, J.-W., Lentz, D., Ren, Z., Zhao, X.-F., Deng, X.-D., Hall, D., 2014. Dissolution–reprecipitation process of magnetite from the Chengchao iron deposit: Insights into ore genesis and implication for *in-situ* chemical analysis of magnetite. Ore Geol. Rev. 57, 393–405.

Huang, X.-W., Beaudoin, G., 2019. Textures and chemical composition of magnetite from iron oxide-copper-gold (IOCG) and Kiruna-type iron oxide-apatite (IOA) deposits and their implications for ore genesis and magnetite classification schemes. Econ. Geol. 114, 953–979.

Huang, X.-W., Beaudoin, G., 2021. Nanoinclusions in zoned magnetite from the Sossego IOCG deposit, Carajás, Brazil: Implication for mineral zoning and magnetite origin discrimination. Ore Geol. Rev. 139, 104453.

Huang, X.-W., Boutroy, É., Makvandi, S., Beaudoin, G., Corriveau, L., De Toni, A.F., 2019. Trace element composition of iron oxides from IOCG and IOA deposits: relationship to hydrothermal alteration and deposit subtypes. Miner. Deposita 54 (4), 525–552.

Huang, X.-W., Zhou, M.-F., Beaudoin, G., Gao, J.-F., Qi, L., Lyu, C., 2018. Origin of the volcanic-hosted Yamansu Fe deposit, Eastern Tianshan, NW China: constraints from pyrite Re-Os isotopes, stable isotopes, and in situ magnetite trace elements. Miner. Deposita 53 (7), 1039–1060.

Ilton, E.S., Eugster, H.P., 1989. Base metal exchange between magnetite and a chloride-rich hydrothermal fluid. Geochim. Cosmochim. Acta 53 (2), 291–301.

Knipping, J.L., Bilenker, L.D., Simon, A.C., Reich, M., Barra, F., Deditius, A.P., Wälle, M., Heinrich, C.A., Holtz, F., Munizaga, R., 2015. Trace elements in magnetite from massive iron oxide-apatite deposits indicate a combined formation by igneous and magmatic-hydrothermal processes. Geochim. Cosmochim. Acta 171, 15–38.

Liu, P.-P., Zhou, M.-F., Chen, W.T., Gao, J.-F., Huang, X.-W., 2015. In-situ LA-ICP-MS trace elemental analyses of magnetite: Fe–Ti–(V) oxide-bearing mafic–ultramafic layered intrusions of the Emeishan Large Igneous Province. SW China. Ore Geol. Rev. 65, 853–871.

Meinert, L.D., Dipple, G.M., Nicolescu, S., 2005. World skarn deposits. In: Hedenquist, J. W., Thompson, J.F.H., Goldfarb, R.J., Richards, J.P. (Eds.), Economic Geology 100th Anniversary Volume. Society of Economic Geologists, Littleton, Colorado, pp. 299–336.

Nadoll, P., Angerer, T., Mauk, J.L., French, D., Walshe, J., 2014. The chemistry of hydrothermal magnetite: A review. Ore Geol. Rev. 61, 1–32.

Putnis, A., 2009. Mineral replacement reactions. Rev. Mineral. Geochem. 70 (1), 87–124.

Putnis, A., 2015. Transient porosity resulting from fluid–mineral interaction and its consequences. Rev. Mineral. Geochem. 80 (1), 1–23.

Ronzê, P.C., Soares, A.D.V., dos Santos, M.G.S., Barreira, C.F., 2000. Alemão copper-gold (U-REE) deposit, Carajás, Brazil. In: Poter, T.M. (Ed.), Hydrothermal iron oxide copper-gold & related deposits: a global perspective. PGC Publishing, Adelaide, pp. 191–202.

Simon, A.C., Knipping, J., Reich, M., Barra, F., Deditius, A.P., Bilenker, L., Childress, T., 2018. Kiruna-Type Iron Oxide-Apatite (IOA) and Iron Oxide Copper-Gold (IOCG) Deposits Form by a Combination of Igneous and Magmatic-Hydrothermal Processes: Evidence from the Chilean Iron Belt. Economic Geology Special Publications 21, 89–114.

Watson, E.B., 1996. Surface enrichment and trace-element uptake during crystal growth. Geochim. Cosmochim. Acta 60 (24), 5013–5020.

Watson, E.B., Lanzillo, N.A., Nayak, S.K., 2011. The Growth Entrapment Model (GEM): New Insights from Molecular-Scale Simulations of Ti in Quartz. AGU Fall Meeting Abstracts, p. PP51E-04.

Williams, P.J., Barton, M.D., Johnson, D.A., Fontbote, L., De Haller, A., Mark, G., Oliver, N.H.S., Marschik, R., 2005. Iron oxide copper-gold deposits: geology, space-time distribution and possible modes of origin. In: Hedenquist, J.W., Thompson, J.F. H., Goldfarb, R.J., Richards, J.P. (Eds.), Economic Geology 100th anniversary volume. Society of Economic Geologists, Littelton, Colorado, USA, pp. 371–405.

Yin, S., Ma, C., Robinson, P.T., 2017. Textures and high field strength elements in hydrothermal magnetite from a skarn system: Implications for coupled dissolution-reprecipitation reactions. Am. Mineral. 102, 1045–1056.

Yin, S., Wirth, R., Ma, C., Xu, J., 2019. The role of mineral nanoparticles at a fluid-magnetite interface: Implications for trace-element uptake in hydrothermal systems. Am. Mineral. 104, 1180–1188.

Zhou, H., Sun, X., Cook, N.J., Lin, H., Fu, Y.u., Zhong, R., Brugger, J., 2017. Nano-to micron-scale particulate gold hosted by magnetite: A product of gold scavenging by bismuth melts. Econ. Geol. 112 (4), 993–1010.

Zhou, H., Wirth, R., Gleeson, S.A., Schreiber, A., Mayanna, S., 2021. Three-Dimensional and Microstructural Fingerprinting of Gold Nanoparticles at Fluid-Mineral Interfaces. Am. Mineral. 106, 97–104.